

Marine ice formation in a suture zone on the Larsen C Ice Shelf and its influence on ice shelf dynamics

Daniela Jansen,^{1,2} Adrian Luckman,¹ Bernd Kulessa,¹ Paul R. Holland,³ and Edward C. King³

Received 22 February 2013; revised 9 July 2013; accepted 25 July 2013; published 30 August 2013.

[1] Antarctic ice shelves are fed primarily by the glaciers flowing into them. Downstream of promontories separating these glaciers, supercooled water can rise and freeze into suture zones, leading to the accretion of marine ice. Marine ice bodies have been found in several Antarctic ice shelves, but little is known about their detailed geometry, rate of accretion, or influence on ice dynamics. In this study, we investigate marine ice in a suture zone downstream of the Joerg Peninsula in the southern part of the Larsen C Ice Shelf, Antarctic Peninsula. We present ground penetrating radar data from which we infer the base of the meteoric ice and, in combination with GPS data and assuming hydrostatic equilibrium, estimate marine ice thickness within a suture zone. We show that the Joerg Peninsula suture zone contains marine ice layer, which is increasing in thickness along flow from ~140 m to 180 m over 20 km, implying an average basal accretion rate of ~0.5 m a⁻¹ in our study area. We examined the impact of this inferred marine ice on ice shelf dynamics by modeling the suture zone within an ice flow model. The results, which replicate observed surface velocities and strain rates, show that the warmer and thus softer ice of the suture zone serves to channel shear deformation. This enables decoupling of neighboring flow units with different flow velocities, while maintaining the structural integrity of the ice shelf.

Citation: Jansen, D., A. Luckman, B. Kulessa, P. R. Holland, and E. C. King (2013), Marine ice formation in a suture zone on the Larsen C Ice Shelf and its influence on ice shelf dynamics, *J. Geophys. Res. Earth Surf.*, 118, 1628–1640, doi:10.1002/jgrf.20120.

1. Introduction

[2] Ice accreted to the base of ice shelves by freezing of sea water, otherwise known as marine ice, has been found beneath several ice shelves around Antarctica [Thyssen, 1988; Morgan, 1972; Craven *et al.*, 2009; Khazendar *et al.*, 2009; Holland *et al.*, 2009; Neal, 1979; Khazendar *et al.*, 2001; Tison *et al.*, 2001; Tison *et al.*, 1998]. The accretion process is an essential part of the ice-ocean interaction in the cavity and of the mass balance of some ice shelves. In the case of the Amery Ice Shelf, the marine ice layer extends all the way to the calving front [Craven *et al.*, 2009] and is sometimes detected in icebergs calved there from Warren *et al.* [1993], while at the Ronne Ice Shelf most of the marine ice layer is lost due to enhanced basal melting in the vicinity of the calving front [Oerter *et al.*, 1992]. The main source of marine ice is the deposition of frazil ice crystals at the base of an ice shelf. The pressure dependency of the melting point

of ice leads to enhanced melting at the grounding line where the ice draft is usually at a maximum. The fresh supercooled melt water is more buoyant than the surrounding water and thus flows upward along the base of the ice shelf. Frazil ice, generated from this supercooled melt water as it rises, accumulates where the overlying ice is thinner and the water pressure is reduced, and compaction may generate marine ice [Lewis and Perkin, 1986; Bombosch and Jenkins, 1995]. The accumulated ice is formed at the melting point of seawater and is thus warm in comparison to the meteoric ice above [e.g., Paterson, 1994; Craven *et al.*, 2009]. This accretion process can be active in large areas of lower draft and smooth subsurface topography if the supply of supercooled melt water is sufficient, such as in the central part of the Ronne Ice Shelf [Thyssen, 1988]. Marine ice originating from deposition of frazil ice crystals has also been observed in ice shelf rift systems, where it can contribute to what is referred to as an “ice mélange,” which also contains debris from the rift shoulders [e.g., MacAyeal *et al.*, 1998; Tison *et al.*, 2001; Khazendar *et al.*, 2001; Khazendar and Jenkins, 2003; Pattyn *et al.*, 2012].

[3] Holland *et al.* [2009] demonstrated that the Larsen C Ice Shelf (LCIS) contains marine ice concentrated in narrow zones originating downstream of promontories. These so-called suture zones delineate the boundaries of ice shelf flow units coming from the inlets feeding the central part of the ice shelf. Suture zones stand out on satellite imagery due to their smooth surface in comparison to the neighboring flow units,

¹College of Science, Swansea University, UK.

²Now at Alfred Wegener Institute Helmholtz Centre for Polar and Marine Research, Bremerhaven, Germany.

³British Antarctic Survey, Cambridge, UK.

Corresponding author: D. Jansen, Now at Alfred Wegener Institute Helmholtz Centre for Polar and Marine Research, Am Handelshafen 12, DE-27570 Bremerhaven, Germany. (daniela.jansen@awi.de)

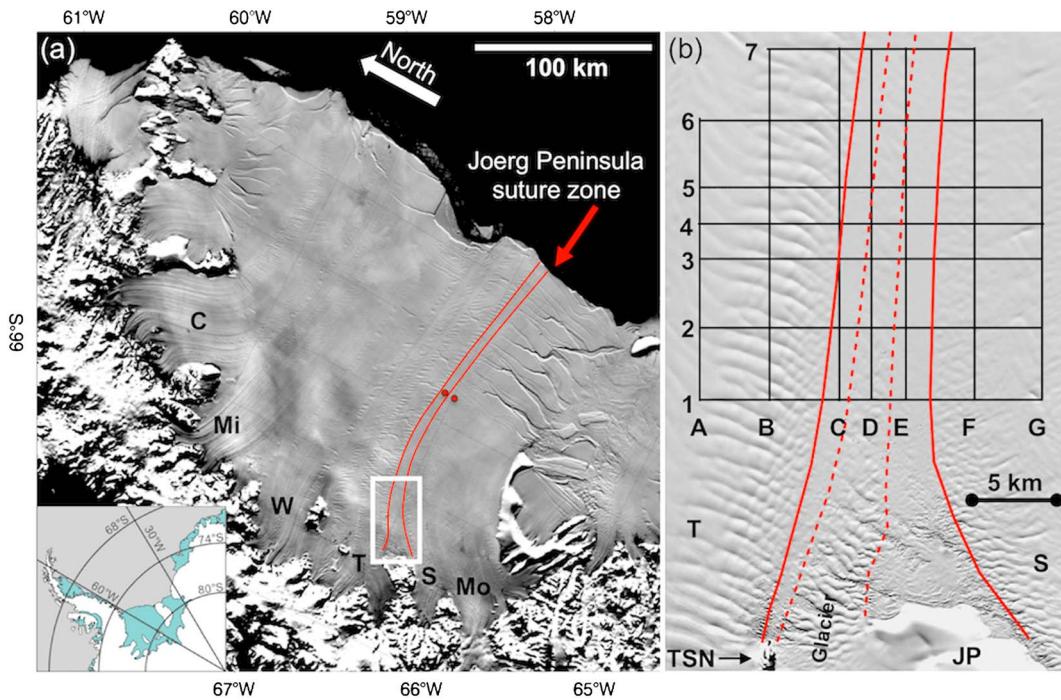


Figure 1. (a) Larsen C Ice Shelf, Antarctic Peninsula. The white rectangle shows the location of Figure 1b. Background image is the MODIS Mosaic of Antarctica (MOA) [Haran *et al.*, 2005]. Red dots: position of seismic CMP surveys; C: Cabinet Inlet; Mi: Mill Inlet; W: Whirlwind Inlet; T: Trail inlet; S: Solberg Inlet; Mo: Mobile Oil Inlet. (b) Survey area and location of the radar lines (black lines). Red dots indicate the positions of radar CMP surveys. Red solid lines delineate the suture zone; the dashed lines enclose the glacier fragments from the peninsula. TSN: Three Slice Nunatak; JP: Joerg Peninsula. The background image is Landsat, 22 November 2001. The ice flow direction is marked by elongated surface features reaching from the grounding line to the calving front.

which are mostly fractured at their margins [Luckman *et al.*, 2012; McGrath *et al.*, 2012]. The results of Holland *et al.* [2009] were based on the hypothesis that the absence of basal reflections in airborne ice penetrating radar surveys is an indication for marine ice at the ice shelf base. The missing reflections from the marine ice-ocean interface can be explained by the high dielectric absorption of the saline ice [Thyssen, 1988]. The transition from marine ice to ocean water may be on a spectrum spanning frazil ice, slushy ice, and fully consolidated ice, as observed in ice cores on the Ronne Ice Shelf and Amery Ice Shelf [Treverrow *et al.*, 2010; Craven *et al.*, 2009; Oerter *et al.*, 1992]. Although the extent and relative proportion of mass of the marine ice bodies in LCIS are smaller than those in the Ronne or Amery Ice Shelf, these elongated zones play an important role for ice shelf stability, as they appear to prevent the propagation of lateral rifts [visible in Figure 1; Holland *et al.*, 2009; Glasser *et al.*, 2009].

[4] Here we investigate a suture zone in the LCIS to better understand the extent, thickness, and likely accumulation rates of marine ice in such areas, and to examine its influence on the flow regime. We present geophysical field data collected in a 20 km × 20 km grid sampled at 4 km spacing at the origin of a suture zone. These data include Ground Penetrating Radar (GPR) profiles along and across flow to map the basal boundary of the meteoric ice layer, and differential Global Positioning System (dGPS) data to measure the surface elevation along these profiles. By combining these

two data sets and assuming that the ice shelf is in hydrostatic equilibrium, we are able to map the extent of a marine ice layer in the Joerg Peninsula suture zone and to determine its thickness. We use the newly derived ice thickness data of the meteoric and marine layer as boundary conditions for a numerical ice shelf model, and quantify the influence of this marine ice layer on the flow regime downstream of the Joerg Peninsula.

2. Study Area and Setup of Field Survey

[5] The LCIS is the largest ice shelf of the Antarctic Peninsula with an area of ~51,000 km² [Cook and Vaughan, 2010], and a north-south extent of ~300 km. It consists of clearly distinguishable flow units [Glasser *et al.*, 2009] with the main ones originating from Cabinet Inlet, Mill Inlet, and Whirlwind Inlet (from north to south, Figure 1), and the Mobil Oil Inlet with the highest inflow velocities [e.g., Jansen *et al.*, 2010; Rignot *et al.*, 2011].

[6] Our study area (Figure 1) is located on the transition between two smaller inlets in the southern part of the ice shelf. The Joerg Peninsula, a promontory extending ~40 km into the ice shelf, divides the Trail Inlet (north) and the Solberg Inlet (south). There is some discharge from a smaller glacier on the peninsula itself, but most of the ice shelf directly downstream of the peninsula must be formed in situ, partly from surface accumulation and compaction, and partly from the basal accretion of marine ice. Another smaller

obstacle to ice flow a few kilometers north of the main peninsula, Three Slice Nunatak, defines the northern boundary of this suture zone. The ice discharge from the peninsula gives the suture zone a three-lobe structure [also *Holland et al.* 2009], with smooth flow bands in the north and south and heavily fractured glacier ice blocks in the center, which is clearly distinguishable in satellite data (Figure 1).

[7] During November and December 2009, we carried out a field campaign using GPR and dGPS to investigate the structure of the ice shelf close to the region of origin of the suture zone ice (Figure 1). Significant surface crevassing made it impossible to extend the measurements closer to the grounding line so the GPR profiles start approximately 10 km downstream of Joerg Peninsula and Three Slice Nunatak. The radar profiles were arranged as a rectangular grid of 20 km × 20 km, with corners omitted in the downstream direction as a result of time constraints. The gridlines are approximately orientated parallel and perpendicular to the flow direction, which is directed eastward in this area of the ice shelf, parallel to the suture zone. The spacing between the grid lines is 4 km, with two extra profiles (one across and one along flow) in the center of the grid to improve the sampling to 2 km across the suture zone ice. Three common midpoint (CMP) radar surveys were carried out on the neighboring flow units and on the suture zone (Figure 1b). The flow-parallel radar profiles will be referred to as A–G from north to south (left to right in the map, Figure 1b) and the flow-perpendicular profiles are named 1–7 from west to east (bottom to top in Figure 1b).

3. Methods

3.1. GPR

[8] The common-offset 50 MHz data were acquired using a Pulse-Ekko PE100 GPR system towed behind a snow-scooter. The stacked GPR waveforms were recorded every 3 s using eight stacks, yielding an average trace spacing of ~4.3 m. The raw GPR data were processed using standard techniques implemented in the software package ReflexW, including automatic gain control, band-pass filtering, and correction for surface topography as recorded by dGPS. Basal reflectors were picked where possible on each radar profile to derive the thickness of the meteoric ice layer. In addition to the radar profiling, three CMP surveys were carried out at the intersections of radar line 5 with three flow-parallel radar lines (Figure 1). Using the software ReflexW, we performed a semblance analysis to derive a vertical radar-wave velocity model, which enables the conversion of two-way travel time to depth.

3.2. dGPS

[9] Precise planimetric and height location of the radar system was recorded with a differential Leica System 1200 GPS. The radar traces were geolocated by means of the dGPS data collected simultaneously, tied together by recording time. The dGPS data were processed using the software Leica GeoOffice. By processing the data relative to the GPS base-station in the center of the radar grid, tidal influences on the elevation measurements were minimized. Although elevation changes due to ocean tides on ice shelves elevation are spatially variable, the distances (< 14 km) between moving

and stationary GPS receivers are short enough not to introduce a significant differential tidal amplitude. To transform the dGPS elevation into ice shelf freeboard, two other corrections are necessary. First, to correct for the geoid, we used the Eigen-6 model [*Förste*, 2011], which is based on GRACE data from a model distributed by the International Centre for Global Earth Models (ICGEM, <http://icgem.gfz-potsdam.de/ICGEM>). The correction applied for our survey area amounts 10.5 m. Second, the dynamic ocean topography (DOT) represents the difference between sea surface and geoid, caused by salinity variations and ocean currents. To correct for DOT, we use a model based on GRACE data [*Chambers*, 2006]. In the western Weddell Sea in front of the LCIS, the mean ocean surface is located 1.35 m below the geoid. Possible error sources for the dGPS elevation data will be discussed in section 4.5.

3.3. Marine Ice Thickness Calculation

[10] Marine ice has a higher dielectric conductivity than meteoric ice because of its brine content, and this causes the radar waves to be attenuated rather than reflected back to the receiver [*Holland et al.*, 2009; *Thyssen*, 1988]. This explains the missing basal reflection in the radar data used by *Holland et al.* [2009] and means that the base of the marine ice layer cannot be mapped with GPR. Therefore, its thickness has to be determined indirectly. If the thickness of the meteoric ice layer is known from the radar survey and surface elevation is provided by the simultaneous dGPS survey, the marine ice thickness can be calculated under the assumption that the system is in hydrostatic equilibrium [*Thyssen*, 1988; *Fricker et al.*, 2001] using the relation:

$$H_m = \frac{H(\bar{\rho}_i - \rho_w) + h\rho_w}{\rho_w - \rho_m} \quad (1)$$

[11] Where H_m is the thickness of the marine ice layer, H the thickness of the meteoric ice layer, ρ_i the mean density of the meteoric ice layer, ρ_w the density of seawater, h the ice shelf freeboard or corrected elevation, and ρ_m the density of marine ice. We assumed ρ_w to be 1028 kg m⁻³, and ρ_m to be 920 kg m⁻³, which is slightly higher than the value usually used for consolidated ice, as marine ice has on average a low brine content and does not contain any air bubbles [*Oerter et al.*, 1992]. It is important to state here that using this reference density results in a marine ice thickness equivalent for consolidated ice [*Craven et al.*, 2009]. The mean density of the overlying meteoric ice layer $\bar{\rho}_i$ is calculated separately for each location from a vertical density profile for the Solberg flow unit derived from seismic measurements [Figure 1a; see *Jansen et al.*, 2010], which is assumed to be spatially constant.

[12] The assumption of hydrostatic equilibrium may not hold on the margins of the suture zone ice, where stress bridging might influence the freeboard of the ice shelf. Flexural stresses at the suture zone boundary may exist, but are small in comparison to the stresses in the grounding zone of the ice shelf, as the ice on either side of the suture zone boundary is floating. Thus, we make the assumption that flexural stresses are negligible at a distance of twice the ice thickness away from the boundary.

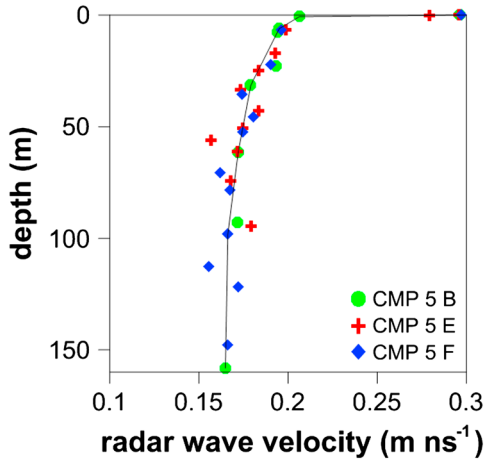


Figure 2. Results of the semblance analysis, showing the vertical profile of the radar-wave velocity in the ice column. The data is color coded to distinguish the three different locations, the intersections of radar line 5 with radar lines B, E, and F (Figure 1b).

3.4. Ice Shelf Model

[13] As marine ice is formed at a temperature close to the pressure melting point of seawater, it is relatively warm in comparison to the ice elsewhere in the ice shelf. This leads to the characteristic vertical temperature profile for ice shelves that experience basal accretion [e.g., Paterson, 1994]. Temperature logs from the Amery Ice Shelf [Craven *et al.*, 2009] show that this higher temperature of around -2°C can be retained during advection downstream, since the marine ice is insulated from the colder surface by the meteoric ice above it. Temperature has a strong influence on the rheological softness of the ice and leads to a lower flow rate factor in Glen’s flow law [Glen, 1955] which describes the empirical relation between stress and strain within ice [Paterson, 1994; Khazendar *et al.*, 2009]. Although other factors, such as impurities or lack of air bubbles, can make marine ice harder than meteoric ice at the same temperature, the difference in temperature makes it significantly softer [Khazendar *et al.*, 2009; Dierckx and Tison, 2013].

[14] The presence of softer ice of marine origin has been shown to have an influence on ice shelf flow, for example as the filling of large rift systems [Larour *et al.*, 2005; MacAyeal *et al.* 1998] and within the highly irregular Brunt/Stancomb-Wills system [Khazendar *et al.*, 2009]. In our study, we investigate the influence of marine ice in a narrow suture zone which connects neighboring flow units and thus may have a significant influence on the coupling between them.

[15] To investigate the influence of the marine ice layer on ice dynamics of the Joerg Peninsula suture zone, we use a numerical ice shelf model. The continuum-mechanical flow model [Sandhäger, 2000; Sandhäger *et al.*, 2005; Grosfeld and Sandhäger, 2004] is based on a finite difference numerical implementation that simulates ice-shelf evolution as controlled by ice dynamics and variable environmental boundary conditions. It was applied successfully to the Larsen B and C Ice Shelves [Sandhäger *et al.*, 2005; Jansen *et al.*, 2010] and validated by observations. Gravitational driving forces and

associated stresses are implemented, while, following the approach of MacAyeal *et al.* [1986], friction at the ice shelf-ocean boundary and vertical shear strain due to bending forces are neglected. The ice-shelf body is assumed to be in hydrostatic equilibrium and the horizontal flow velocities are depth invariant, but a realistic vertical temperature and density profile are implemented. In the vertical dimension, the model domain is divided into 13 layers, scaled by the ice thickness. Vertical integration of the flow rate factor then allows the temperature profile to control ice softness, an essential component if warm marine ice layers are present.

4. Results

4.1. CMP Survey

[16] Using the software ReflexW, we performed a semblance analysis to derive a vertical radar-wave velocity model. Figure 2 shows the in situ radar-wave velocities with depth. The CMP survey covered the Solberg Inlet in the south (F5), Trail Inlet in the north (B5), and the suture zone ice in between (E5). For the CMP survey on the suture zone ice, no signal was received beyond a depth of 94 m. Using all data points and the assumption that radar-wave velocity in solid ice is 0.168 m ns^{-1} , we calculated a mean velocity profile (Figure 2). The velocity model was then used to transform the two-way travel times for the picked reflections into ice thickness.

4.2. Grid Profiles Along Flow

[17] The measurement grid consists of seven flow-parallel and seven flow-perpendicular profiles (Figure 1). GPR data from the full lengths of gridlines F and 6, and from parts of some other lines were not considered of good enough quality for subsequent calculations, although the dGPS data collected on all lines were used for a gridded version of the surface elevation. Of the flow-parallel lines, four were entirely located on flow units emerging from Trail (A and B) and Solberg (F and G) Inlets, two lines were located entirely on the suture zone ice (D and E), while line C crosses the northern boundary of the suture zone and covers ice from both the suture zone and Trail Inlet.

[18] Radar lines A and B (not shown) show clear reflections from a relatively smooth base of the ice shelf, disrupted by regular basal crevasses, which also show an expression in the surface elevation with an average dip of 5 m above the center of the crevasse [for a detailed discussion of radar line B, see Luckman *et al.*, 2012]. For profile A, the ice thickness within the noncrevassed parts of the flow units decreases along flow at a rate of approximately 1 m km^{-1} . Of the profiles located on the Solberg Inlet, only one was of sufficient quality for subsequent analysis. Satellite imagery shows that the ice shelf has been fractured heavily when passing the Joerg Peninsula and the resulting rougher base probably leads to dissipation of the radar energy. In contrast to profiles A and B, profile G lacks the smooth reflector at the ice shelf base and only separate reflection hyperbola apexes could be picked from this radar line. The ice thickness varies periodically between 290 m and 325 m while the profile crosses several features that are interpreted as basal crevasses. It is not possible to quantify the strain thinning within this flow unit due to the variability of the thickness.

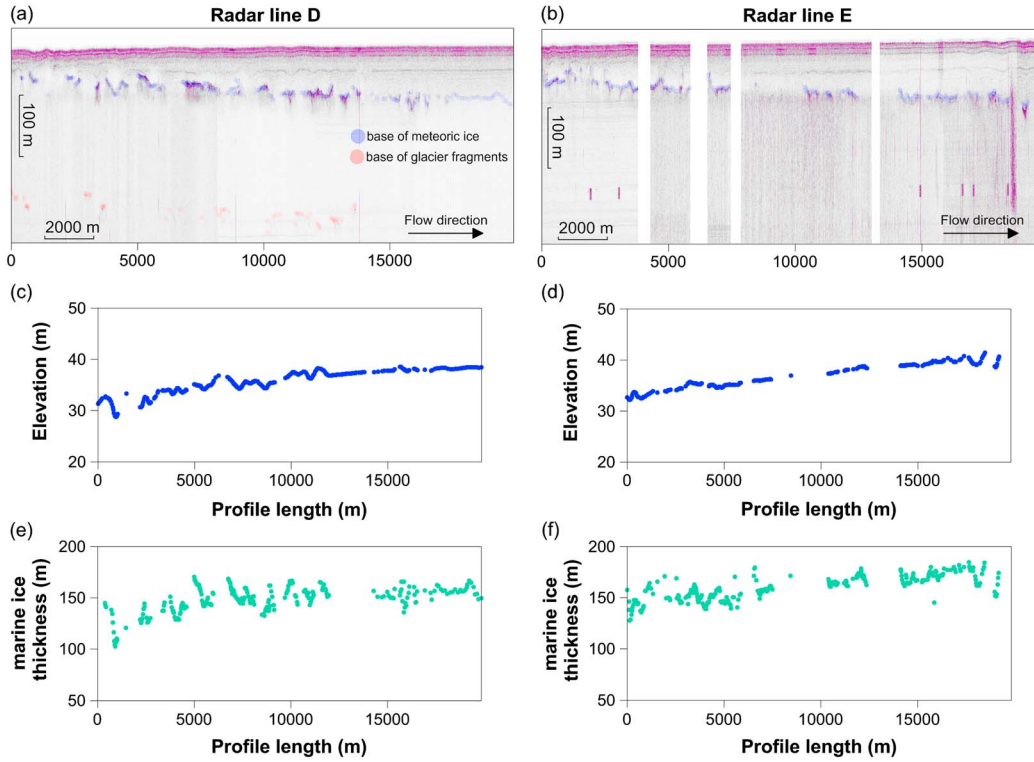


Figure 3. (a) Radargram of radar line D. (b) Radargram of radar line E. In the white gaps, either no radar or faulty GPS data were recorded. Ice flow direction is from left to right on both panels. Color-coded dots show the positions of the picked reflections from the meteoric ice base (blue), the base of the ice blocks from the glacier on the peninsula (red). (c) Surface elevation for radar line D. (d) Surface elevation for radar line E. (e) Calculated marine ice thickness for radar line D. (f) Calculated marine ice thickness for radar line E.

[19] Radar profile D (Figure 3a), located in the center of the suture zone, shows reflections from the base of ice blocks originating from the glacier on the Joerg Peninsula, alternating with an upper reflector that we interpret as the boundary between the locally accumulated meteoric ice and marine ice. The upper reflector is very strong and consists of short continuous traces, whereas the reflections from the base of the glacier ice blocks occur as isolated reflection hyperbolae. The meteoric/marine ice boundary dips along the profile as would be expected of an ice body advecting toward the calving front while accumulating snow on its upper surface. Because the ice flow in Figures 3a and 3b is from left to right, the x axis provides a proxy for time and shows the suture zone at different stages in its development. The elevation increases along flow by 10.3 m in 20 km (Figure 3c). Toward the end of the profile, the deep reflectors are no longer present as the line leaves the central area of the suture zone containing the meteoric ice sections. This is also reflected in a smoother elevation profile (Figure 3c). The meteoric/marine ice boundary remains visible in the data, but the reflection is much weaker than in the upstream section. Using equation (1), we calculated the thickness of the marine ice layer in the gaps between the glacier ice blocks, shown in Figure 3e. The mean thickness increases from 120 m at the landward to 160 m at the seaward end of the profile, with a range of ± 10 m. The increase in marine ice thickness is strongest in the first third of the profile,

although it should be noted that the radar line does not uniformly sample the center of the suture zone.

[20] Radar line E (Figure 3b) does not cross any of the two neighboring meteoric flow units and lies entirely in the southern part of the suture zone. The basal reflector is much weaker than in the first part of line D, but it is continuous for longer stretches and also dips along flow. The elevation rises along flow (Figure 3d) and the marine ice thickness increases from 140 m at the start of the profile to 180 m at the end (Figure 3f).

4.3. Across Flow Profiles

[21] The radar lines across the suture zone perpendicular to ice flow show that there is a steep transition in the apparent basal reflector between Trail and Solberg Inlets and the suture zone ice, with a step of more than 200 m in depth within a horizontal distance of 500 m (Figures 4a and 4b). All cross profiles show a trough in elevation above the suture zone, ranging from ~ 10 m in profile 1 (Figure 4c) to ~ 4 m in profile 7. The visible layering in the upper ice column shows no contrast in the accumulation patterns between this trough and the adjacent flow units within the survey area. The meteoric ice layer is thinnest in the northern part of the suture zone, which is consistent with the minimum thickness measured in radar line C. The meteoric ice layer thickness increases from radar line to radar line downstream, as is to be expected from the results of the along flow radar lines.

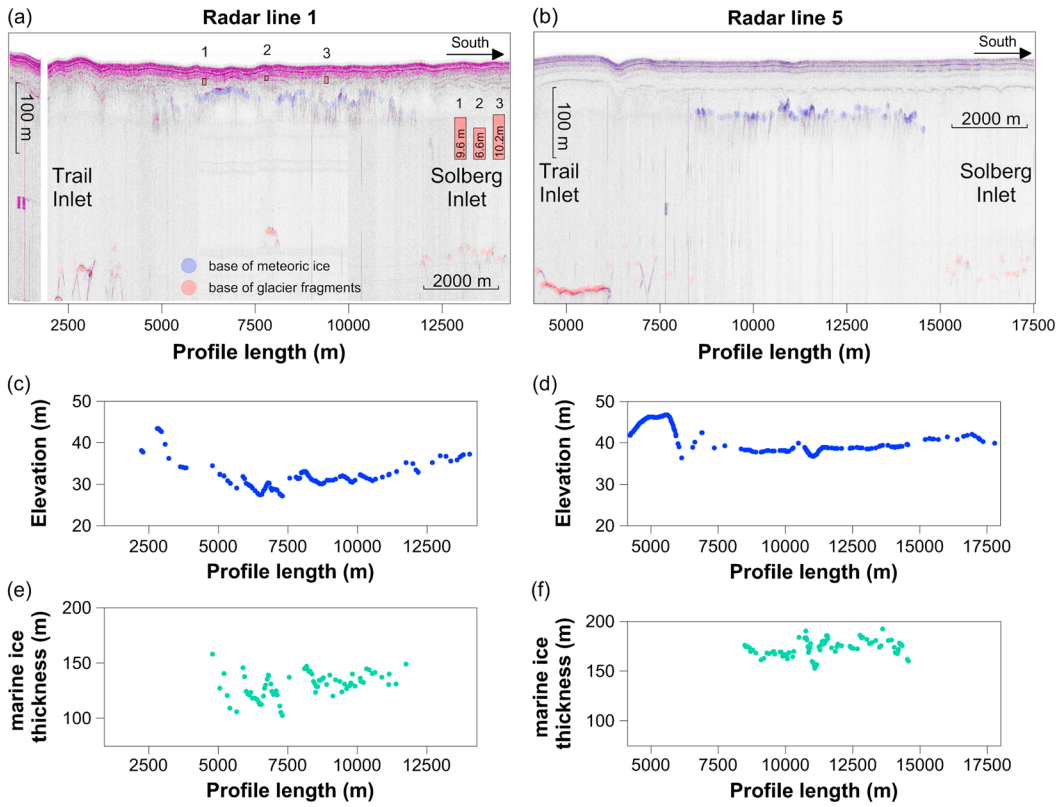


Figure 4. (a) Radargram of radar line 1. The red columns illustrate the thickness variation of a prominent meteoric ice layer on different parts of the suture zone. (b) Radargram of radar line 5. Ice flow direction is into the page on both panels. Color-coded dots show the positions of the picked reflections from the meteoric ice base (blue) and the base of the ice blocks from the glacier on the peninsula or the base of the neighboring flow units (red). (c) Surface elevation for radar line 1. (d) Surface elevation for radar line 5. (e) Calculated marine ice thickness for radar line 1. (f) Calculated marine ice thickness for radar line 5.

For radar line 1 (Figure 4a), located closest to the grounding line, the marine ice thickness varies between 120 m and 140 m (Figure 4e). For radar line 7 (not shown), furthest from the grounding line, the boundary is very smooth and continuous, and the thickness is ~ 200 m, which is the overall maximum within the surveyed area. Figure 4b shows the flow-perpendicular radar line 5, on which all CMP surveys are located. On the ice coming from Trail Inlet, the basal boundary of the ice shelf is a smooth and prominent reflector in the radargram. Toward the margin of the flow unit, the ice base is characterized by occasional single reflections, with the transition being marked by a feature interpreted as a basal crevasse, whose presence is also reflected in the surface topography (Figure 4d). This is consistent with the surface structure of the ice visible on the Landsat image in Figure 1, which shows the margins of the flow units to be broken into small fragments. On the Solberg flow unit, no smooth basal reflector can be detected, which is in agreement with the observations from the flow-parallel lines.

4.4. Gridded Data

[22] The nonuniformly sampled measurements of the geometry of the marine ice within the suture zone were resampled to a uniform grid so that they could be incorporated into a numerical ice shelf model. To be consistent, we independently gridded elevation (Figure 5a) and meteoric ice thickness (Figure 5b) over the sampled area and only then

used these grids to calculate the mean marine ice thickness for the model representation (Figure 6a). For this gridded data set, we removed the data influenced by basal crevasses. As a mean value, the marine ice thickness in the Joerg Peninsula suture zone increases by 40 m within 20 km in the direction of ice flow. The thickness of the meteoric ice layer increases along flow as a result of surface accumulation, and the ratio between meteoric and marine ice within the ice column increases from $\sim 1:3$ at the upstream end of the survey to $\sim 1:2$, 20 km downstream. The locally accumulated meteoric ice layer as well as the calculated marine ice thickness have their overall minimum thickness in the northern part of the suture zone at the landward end of radar line C.

4.5. Error Estimation

[23] The radar and dGPS survey extended over a period of 21 days, during which the ice shelf moved forward about 19 m (average velocity of 300 m a^{-1}) at the survey site. Due to the low gradients in elevation and ice thickness along flow, we did not consider this displacement as relevant.

[24] As the marine ice thickness is estimated in an indirect way and is a function of several other measured parameters, the error for the marine ice thickness is cumulative, resulting from propagation of errors in ice thickness, density, and elevation. We estimate the error for the measured surface elevation to be 1 m, including uncertainties in DOT and the geoid model, as well as the vertical precision for the dGPS

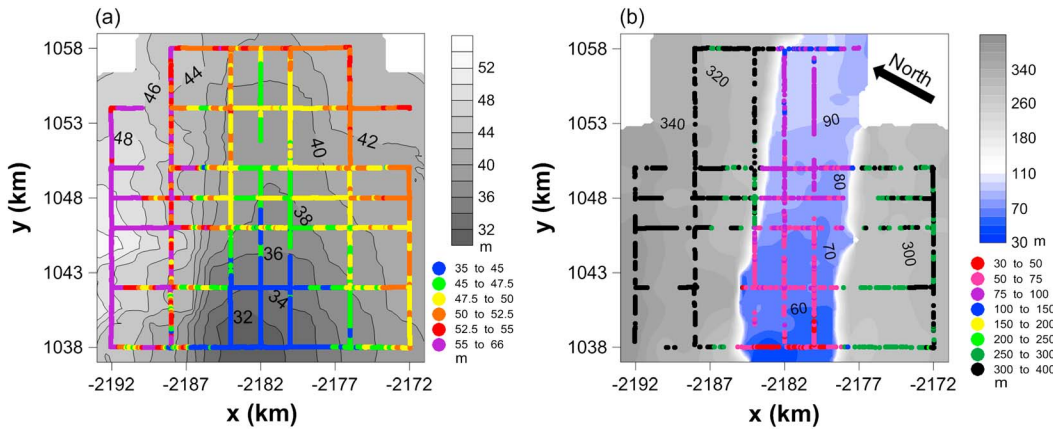


Figure 5. (a) Gridded surface elevation with overlying GPS lines. x and y are in polar stereographic coordinates. (b) Gridded meteoric ice thickness with the locations of picked basal reflectors.

measurements. According to equation (1), this leads to an error E_h of 9.4 m. To quantify the errors in ice thickness due to transforming radar-wave travel time into depth, we calculated the thickness using a lower and upper velocity profile enveloping the data points shown in Figure 2, keeping the values for consolidated ice and snow constant as upper and lower boundaries. This leads to a deviation of $\sim 6\%$ in the mean velocity in the ice column. The resulting Error E_H for marine ice is thus expected to be in the range of 12 m. Error E_ρ due to uncertainties in the depth-integrated density profile are estimated to be ~ 5 m, a value derived from comparison of the density results of four seismic CMP surveys (location Figure 1a) showing deviations of the mean density of the ice column of less than 2%. To further explore the issue of density error, we compared our mean meteoric ice density with a mean density calculated following the firm air method [Holland *et al.*, 2011] based on our GPR data and found the difference to be less than 0.5%. This also supports our hypothesis that the density profile does not change significantly within our survey area. The calculated marine ice thickness according to equation (1) is also sensitive to marine ice density. We are using a reference density of 920 kg m^{-3} , which leads to a marine ice thickness equivalent for

consolidated ice and therefore has no error in the standard sense. Possible influences of the consolidation process of the marine ice will be examined in the discussion.

[25] In total, we assume the error for our marine ice thickness estimate to be in the range of ± 30 m and this value represents the maximum error of the absolute thickness. The relative precision for elevation and ice thickness data and thus also marine ice thickness is significantly better because, on the scale of our measurements, errors for both parameters will be consistent rather than random. The observed 40 m increase in marine ice thickness within our 20 km measurement profile is thus significant.

4.6. Ice Shelf Model Setup and Results

[26] The newly derived ice thickness in the survey area was embedded in the thickness data set we used in previous model simulations [Jansen *et al.*, 2010], which was based on BEDMAP data [Lythe *et al.*, 2001], and blended in at the margins (Figure 7). The model study was restricted to a $25 \text{ km} \times 50 \text{ km}$ area surrounding the Joerg Peninsula suture zone. We chose a high resolution of $200 \text{ m} \times 200 \text{ m}$ per grid cell in order to represent the steep transitions of ice thickness at the boundaries of the suture zone, although our field data

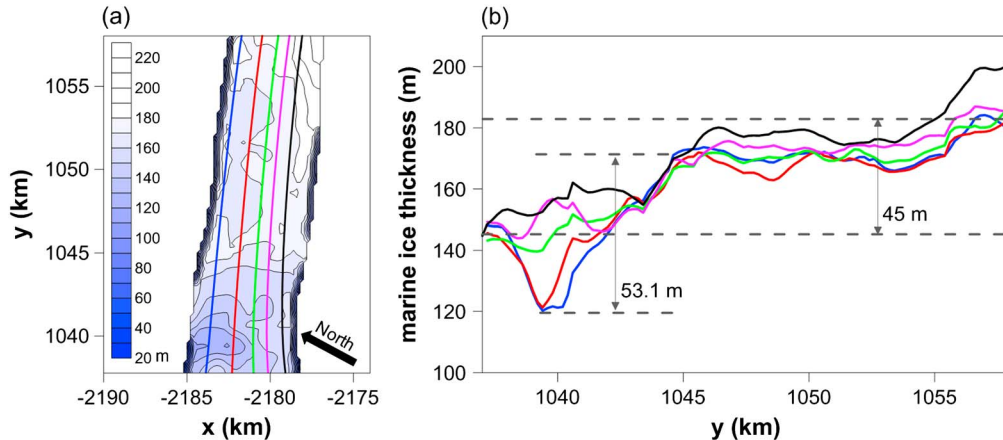


Figure 6. (a) Marine ice thickness grid with flow lines calculated from measured surface velocity [Rignot *et al.*, 2011]. (b) Development of marine ice thickness along the flow lines shown in Figure 6a.

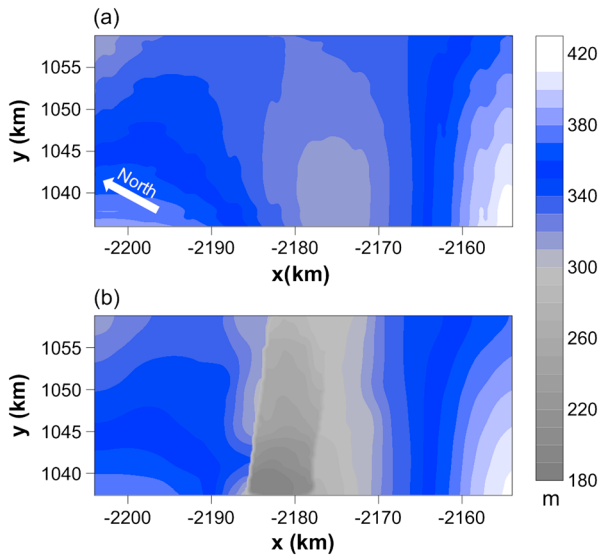


Figure 7. (a) Ice thickness distribution used in former model studies [Jansen et al., 2010]. (b) New total ice thickness (meteoric + marine ice).

does not sample the ice geometry at such high resolution in all dimensions. Surface temperature of the model domain is set to a constant -15.4°C , a value which is below the mean average air temperatures to account for the ice advected from greater heights in the flow units [see also Scambos et al., 2000; Sandhäger et al., 2005]. The surface temperature determines the upper boundary of the vertical temperature profile, which in turn dominates the value of the depth-integrated flow factor, thereby determining the softness of

the ice. The lower boundary of the meteoric ice is set to -2°C , the approximate freezing temperature of seawater at the ice shelf base. The vertical development of the temperature profile is approximated as decreasing proportional to the cube root of depth [Sandhäger et al., 2005]. The marine ice layer is represented as a body of warm ice with a constant temperature at the freezing point of -2°C . This is a reasonable first approximation which ignores the likely presence of a transition zone between cold meteoric ice and the newly accreted marine ice, and a temporal evolution of the temperature profile while the ice is advected toward the calving front [Craven et al., 2005]. Also ignored here is the probably slightly higher temperature of the meteoric ice in the suture zone due to its in situ formation. The marine ice fraction in the ice column is represented by a laterally variable depth-integrated flow factor, depending on the relative proportion of marine ice in the ice column.

[27] The inflow velocities at the boundaries of the model domain are prescribed in orientation and magnitude at the lower boundary (inflow) and both sides. Velocities at the upper boundary are free in magnitude but prescribed in orientation. The model was forced with boundary velocities derived from a model simulation of the entire LCIS [Jansen et al., 2010], which does not include the warm suture zone ice.

[28] In the control model run for an ice shelf with uniform depth-scaled temperature profile and thus a uniform vertically integrated flow factor, the magnitude of the ice flow velocity increases from the lower left corner to the upper right corner of the model domain (Figure 8a). This gradient in the velocity is caused by a higher inflow velocity from Trail Inlet. Shear deformation is smoothly varying within the model domain for this control model run and shows no small-scale anomalies (Figure 8b).

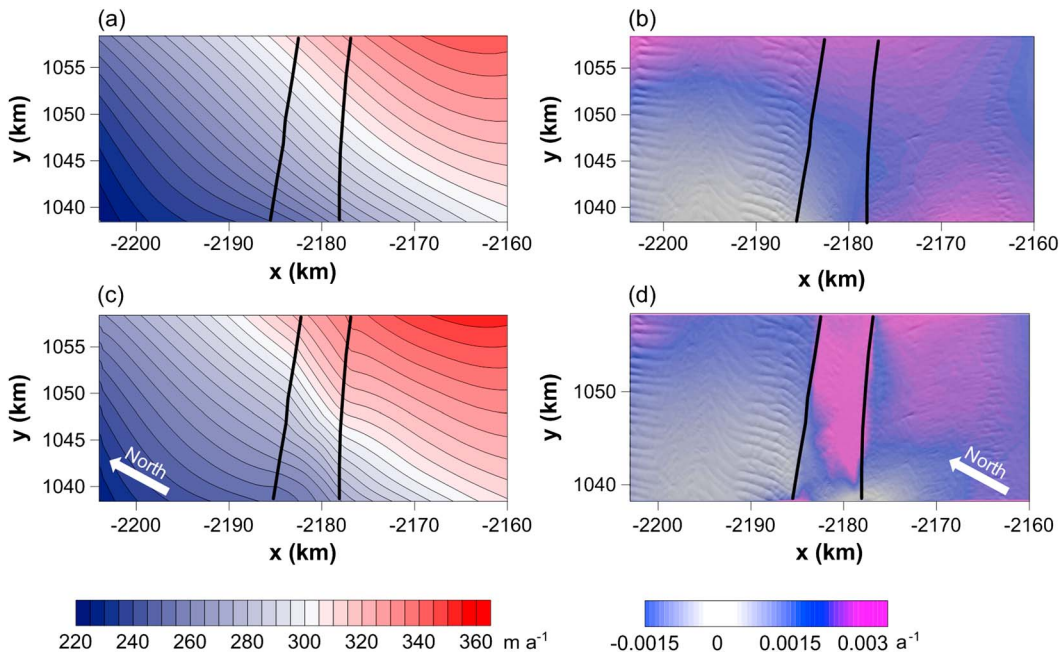


Figure 8. (a) Ice flow velocity for model run without marine ice. (b) Shear strain for the velocity distribution in Figure 8a. Background image in gray scales: Landsat. (c) Ice flow velocity for model run with marine ice. (d) Shear strain for the velocity distribution in Figure 8c. The flow direction is along the suture zone for Figures 8a and 8c.

[29] When the marine ice is introduced into the suture zone in the quantities that we measured, and the spatially variable flow factor is altered accordingly, the modeled flow velocity is significantly affected (Figure 8c). The flow rate factor is constant in the area of pure meteoric ice and varies within the suture zone according to the thickness of the marine ice layer and its relative proportion in the ice column. The soft flow band is visible as an area with a higher velocity gradient across the suture zone. The flow band clearly stands out as an area of enhanced deformation in the shear strain (Figure 8d), whereas the shear strain in the northern flow unit in the direct vicinity of the suture zone is lower in comparison to the control model run (Figure 8b). The shear strain in the southern flow unit has lowered at the lower boundary of the model domain close to the suture zone, whereas the central part appears to be under more strain than in the control run.

5. Discussion

5.1. Origin of GPR Reflector in the Suture Zone

[30] The strong reflector that we observe within the ice column, and which we interpret as the interface between marine and meteoric ice, may have other explanations that we seek to discount here. Such a reflector might also be a result of debris inclusions at the top of the marine ice layer [Nicholls *et al.*, 2012; Eicken *et al.* 1994] or infiltrating permeable meteoric ice with sea water. The latter has been observed in the Wilkins Ice Shelf [Vaughan *et al.* 1993] and is common for sea ice as well in the form of flooding of snow-covered ice floes [e.g., Massom *et al.*, 2001]. In the case of brine infiltration in an ice shelf, a meteoric ice body is present below the reflector and it would therefore be impossible to determine the thickness of a deeper marine ice layer from elevation data. The geometry of the origin of the discussed suture zone, however, shows that there is little inflow of ice at the grounding line at Joerg Peninsula. This implies that the most of the suture zone ice downstream of promontories must have formed in situ, a hypothesis which is supported by the divergence of the observed velocity field shown in Figure 9. The regions immediately downstream of Three Slice Nunatak and Joerg Peninsula highlight divergent flow in the velocity field which shows that in situ accumulation would be necessary to maintain ice thickness or thickening of the ice at the origin of the suture zone. Flooding of snow-covered ice floes might occur close to the grounding line with no inflow, similar to the processes observed in sea ice, but meteoric ice could not reasonably be present underneath as an explanation for our observed surface elevation. The adjacent ice units do not seem to be affected by brine infiltration either, as the strong reflector that we interpret as the base of the meteoric ice is only present within the suture zone. In summary, considering the geometric boundary conditions at the origin of the Joerg Peninsula suture zone, we conclude that the only reasonable explanation of the reflectors we detect is a meteoric-marine ice boundary.

5.2. Marine Ice Thickness Distribution and Derived Freezing Rates

[31] The results from the GPR and dGPS survey close to the origin of the Joerg Peninsula suture zone confirm the presence of marine ice between the Trail and Solberg Inlet, as postulated by Holland *et al.* [2009]. The irregular nature

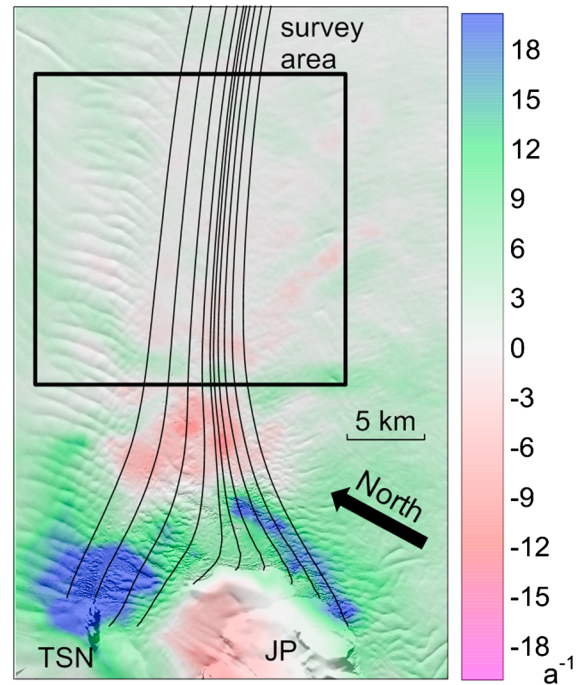


Figure 9. Divergence of the flow velocity in the Joerg Peninsula area [calculated from Rignot *et al.*, 2011]. Positive values indicate divergent flow; negative values indicate convergent flow. Black solid lines indicate the flow path. For location on the ice shelf, see Figure 1.

of the reflector at the boundary between meteoric and marine ice explains the fact that in the lower resolution data used by Holland *et al.* [2009], no reflector was found at the base of the meteoric ice layer. Our higher resolution data captured the base of the meteoric ice layer and thus were able to reproduce the 3D geometry of the marine ice body within the surveyed part of the suture zone.

[32] Comparison of layer thicknesses between two prominent reflectors in the upper ice column of radar line 1 shows that the layer is thicker above the marine ice bodies (Figure 4a). This effect cannot be seen in the radar lines further downstream, as the affected reflectors would be located deeper where no reflectors are recognizable in the radargram. The observation of layer thickening is consistent with the geometrical setting of the suture zone. In the first 5 km downstream from Joerg Peninsula, the suture zone experiences lateral compression caused by the northward movement of the Solberg Inlet flow unit (Figure 1), resulting in a significant narrowing, and thus probably thickening of the suture zone (marine and meteoric) ice. This is also consistent with the divergence of the velocity field, which shows a negative anomaly in the convergent flow area upstream of the survey site (Figure 9). The glacier ice blocks appear to be less affected by the narrowing process, which may be caused by the newly formed suture zone ice being less competent and thereby absorbing more of the compressional stress. The reflector from the meteoric/marine ice boundary is stronger and better defined in the flow-parallel radar lines (Figures 3a and 3b) than in the across-flow lines (Figures 4a and 4b). This anisotropic behavior might be due to the fact that the suture zone ice experiences considerable lateral compaction upstream of

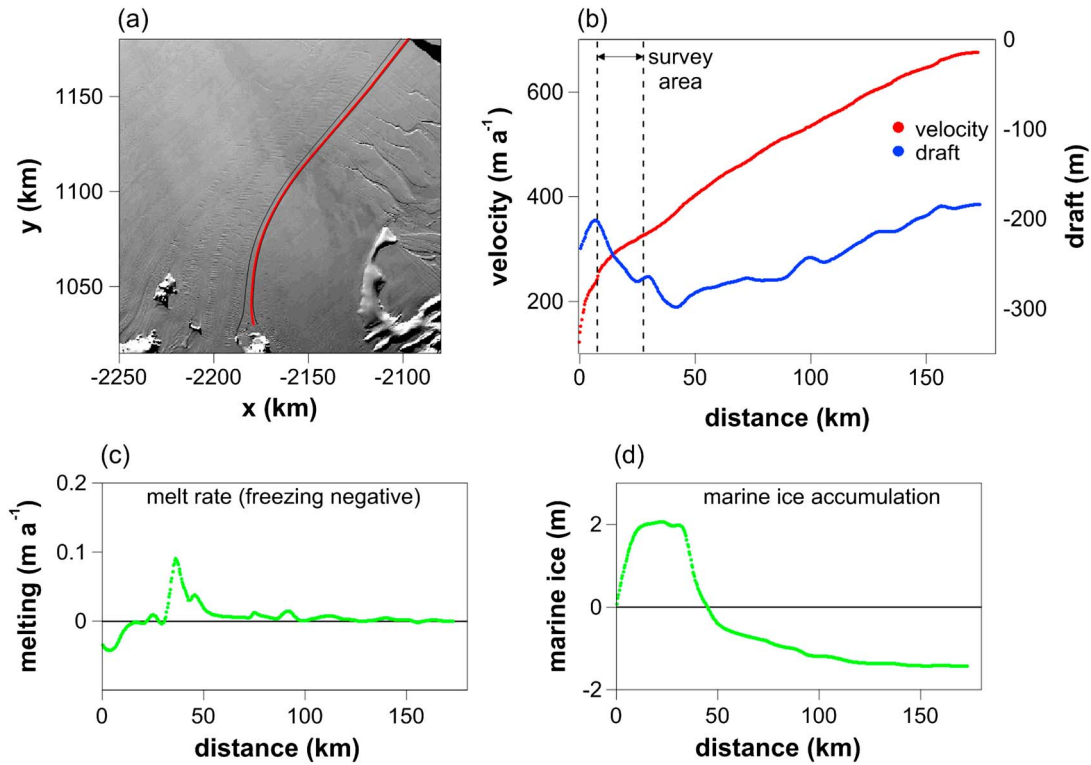


Figure 10. (a) Location of the Joerg Peninsula suture zone and one flow line (red) within its southern part. Background image: MOA [Haran *et al.*, 2005]. (b) Ice shelf draft [blue, from Holland *et al.*, 2009] and flow velocity [red, from Rignot *et al.*, 2011] along the flow line shown in Figure 10a. The dashed lines indicate the position of our survey area within the flow line. (c) Melting/freezing rates along the flow line. (d) Total accumulation/erosion of marine ice. Figures 10c and 10d based on data from an earlier model by Holland *et al.* [2009].

our survey area, a process that might lead to a boundary that is rougher across flow than along flow.

[33] Within the radar grid, the width of the suture zone narrows further by 11%. This is visible in satellite remote sensing imagery and confirmed by calculated flow lines for the boundary of the suture zone on the basis of ice flow velocity data [Rignot *et al.*, 2011]. To confirm that the observed increase in marine ice thickness is not caused by lateral compression, we calculated the mass flux divergence for the survey area from observed velocities and the newly derived ice thickness. We calculated a mean value for the flow units on either side of the suture zone and for the suture zone itself. On the meteoric flow units, the mean value is $\sim -0.1 \text{ m a}^{-1}$ when assuming an accumulation rate of 0.5 m a^{-1} [from model data from Lenaerts *et al.*, 2012], which means that to preserve the current geometry, a basal melt rate of 0.1 m a^{-1} would be necessary. On the suture zone ice, the mean value is $\sim +0.8 \text{ m a}^{-1}$, indicating that an additional 0.8 m a^{-1} ice accumulation would be necessary to preserve geometry. We also calculated a freezing rate from the observed marine ice thickness and travel time of the ice: Using ice flow velocity data [Rignot *et al.* 2011], we found the age difference between the ice entering and leaving the survey area along several flow lines (shown in Figure 6a) to be 74 years. With an overall increase of marine ice layer thickness of 40 m in this same period, the mean basal accretion rate amounts to $\sim 0.5 \text{ m a}^{-1}$ (Figure 6b), which is lower than the value from the mass flux calculations. In the northern part, where the marine ice layer is

thinner, the rates reach values of over 2 m a^{-1} in parts, a variation that allows the initial difference in thickness across the suture zone to be leveled out with the passage of time.

[34] The difference in marine ice thickness between the landward northern and southern suture zone might be caused by the supply of supercooled water. Three Slice Nunatak is located further downstream of the predominant subshef melt water current in the cavity beneath the ice shelf, which is directed along the grounding line in a clockwise manner under the influence of the Coriolis force [Holland *et al.*, 2009; Holland and Feltham, 2006]. The current might be deflected by the Joerg Peninsula, so that less supercooled water reaches the region downstream of Three Slice Nunatak.

[35] The basal accumulation rate we derived from our marine ice layer thickness is a factor of 10 higher than the maximum values predicted from previous modeling in the area of the Joerg Peninsula suture zone [Holland *et al.*, 2009]. That model predicts basal accumulation to be restricted to an area 12 km downstream of the grounding line, accumulating a total amount of marine ice of less than 2 m, being eroded completely by basal melting further downstream (Figure 10). However, geophysical field data [Kulesa *et al.*, 2010] show that a significant amount of marine ice is still present at the base of the suture zone more than 100 km downstream, supporting our results of higher freezing rates and a thicker marine ice layer.

[36] Further support for the magnitude of our marine ice accumulation rate is found in ice thickness data independent

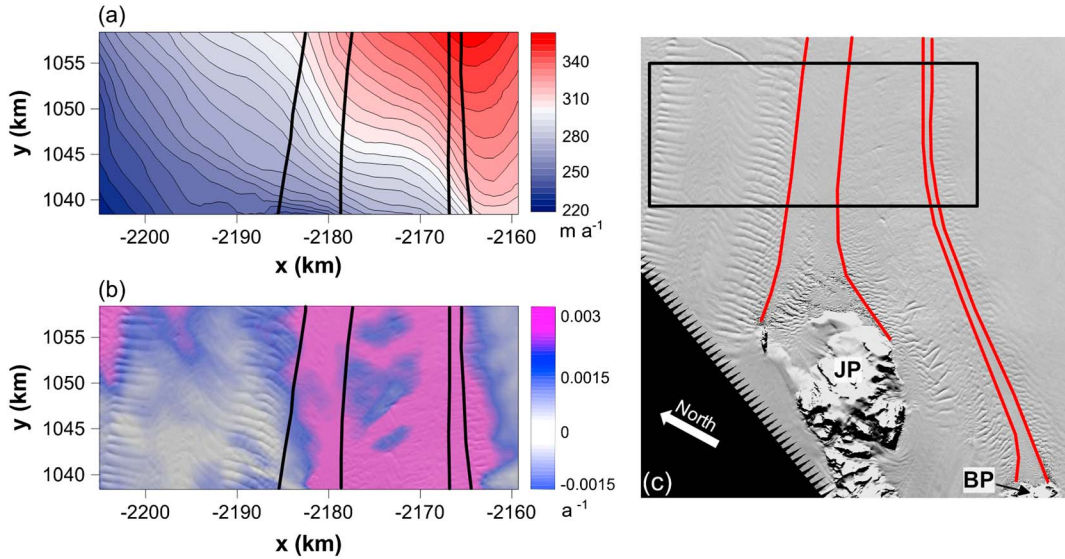


Figure 11. (a) Ice flow velocity magnitude from remote sensing [Rignot *et al.*, 2011]. The black lines indicate the positions of the two suture zones. (b) Shear strain for the velocity distribution in Figure 11a. Background image in gray scales: Landsat. (c) Landsat image showing the positions and origin of the suture zones. JP: Joerg Peninsula; BP: Bermel Peninsula. Flow direction is along the suture zone.

from our measurements. In the data set used by *Holland et al.* [2009], which is based on surface elevation measurements, the ice shelf in the Joerg Peninsula suture zone thickens over the first 50 km, and the ice draft within the area of our radar survey increases downstream by 65 m (Figure 10b). Typically, an ice shelf thins as it flows toward the calving margin in keeping with the velocity gradient. Assuming a surface accumulation of 0.5 m a^{-1} ice equivalent and a mean density of the ice column based on the density profile used for our calculation of marine ice, the 65 m increase of ice shelf draft would correspond to a basal accumulation of 40 m, which is entirely consistent with the increase of marine ice layer thickness that we derive from our measurements. The increasing ice thickness from *Holland et al.* [2009] downstream of our survey area might be an indication for marine ice accretion going on even further.

[37] Little is known about the consolidation process of basally accreted marine ice as it is advected downstream, and observations or sampling of accretion zones are rare. However, in the Amery Ice Shelf [Craven *et al.*, 2005; Craven *et al.*, 2009] as well as in the Ronne Ice Shelf [Oerter *et al.*, 1992], drilling into marine ice showed that the lower layers are permeable and that there is a transition from seawater mixed with ice crystals (“slush”) to fully consolidated ice. Due to the presence of liquid saline water within the permeable layer, the density of marine ice can be significantly higher than for consolidated meteoric ice [Craven *et al.*, 2009]. In our approach [also used by Fricker *et al.*, 2001; Craven *et al.*, 2009], where the amount of marine ice in the ice column is estimated by assuming hydrostatic equilibrium, the resulting thickness is an effective thickness (consolidated ice equivalent) of marine ice contributing to buoyancy. Craven *et al.* [2009] also used a reference density of consolidated marine ice of 920 kg m^{-3} to estimate marine ice thickness between two drilling sites, whereas they found the mean density including the slush layers to be 933 kg m^{-3} and 938 kg m^{-3} . The two drilling sites were located

68 km apart, or in terms of the age of the ice 100 years, and exhibit a decrease of density along flow of 5 kg m^{-3} . This shows that the relative change in density due to the consolidation process along flow is highly unlikely to cause the increase in elevation in our survey area, as it would require a decrease of 30 kg m^{-3} according to equation (1).

[38] Thus, we conclude that the most likely explanation for the evolution of elevation along flow is due to a combination of surface accumulation and ongoing basal accretion of marine ice, although further work is needed in understanding the consolidation process and equating the effective thickness to the actual presence of different stages of consolidation.

5.3. Implications for Ice Shelf Dynamics

[39] In the model, the soft flow band in the suture zone channels the shear strain, which in turn has a relaxing effect on the neighboring flow units in a manner previously detected over wider areas of the Brunt and Fimbul ice shelves [Khazendar *et al.*, 2009].

[40] The channeling of shear deformation can also be observed in remote sensing data for this region (Figure 11a) [Rignot *et al.*, 2011], where the suture zone downstream of the Joerg Peninsula is characterized by high flow-perpendicular gradients in velocity and corresponding high shear strain (Figure 11b). In the velocity and shear strain data, another zone further to the south stands out as an area with high gradients (Figure 11c). Our survey area did not cover this smaller suture zone, but according to *Holland et al.* [2009] it is likely to contain marine ice as well. Due to this second soft suture zone, the Solberg Inlet flow unit is partially decoupled from its neighbors and its center experiences significantly less shear deformation. Thus, the presence of marine ice has a stabilizing effect on the structure of the ice shelf close to the grounding line, as the channeling of shear strain acts to inhibit the growth of shear crevasses in areas where adjacent flow units have different inflow velocities. The suture zone provides a soft

coupling of the stiffer meteoric ice, as shown by inverse modeling [Khazendar *et al.*, 2011]. Within the softer ice bands, shear stress is dissipated by deformation without fracturing, which is apparent from the smooth surface of the suture zones (Figure 11b). This stabilizing effect is most important in the case of large flow-perpendicular gradients in velocity between flow units. In the case of Trail Inlet, weak coupling does not completely prevent shear crevassing [Luckman *et al.*, 2012], but it may serve to lengthen the interval between the opening of crevasses.

6. Conclusions

[41] A geophysical field survey on LCIS has revealed the detailed geometry of a marine ice body within a suture zone near the Joerg Peninsula. Our data show that the thickness of the marine ice requires basal accretion rates that are significantly higher than freezing rates previously predicted by ice-ocean interaction modeling for this area. We also found strong evidence that basal accumulation of marine ice is ongoing over the 20 km survey region, as far as 35 km away from the grounding line. Averaged over 20 km long ice shelf section covered by our survey, the freezing rate amounts 0.5 m a^{-1} , but can reach up to 2 m a^{-1} in some areas. The thickening rate due to basal and surface accumulation along the flow line is in good agreement with an ice thickness profile derived from elevation measurements independent from our data.

[42] Numerical modeling of ice dynamics around Joerg Peninsula suture zone has revealed that warm marine ice can provide a soft coupling between adjacent ice shelf flow units and enable the observed high lateral velocity gradients between them. By channeling shear deformation and thus dissipating shear stress without fracturing, suture zones containing marine ice can lead to a relaxation within the neighboring flow units and prevent or reduce the growth and propagation of shear crevasses, thereby potentially stabilizing the ice shelf in this region.

[43] **Acknowledgments.** This project was funded by the UK Natural Environment Research Council (NERC) (Projects NE/E012914/1 and NE/I016678/1) and the Climate Consortium of Wales (C3W). GPR and GPS equipment was kindly loaned by the NERC Geophysical Equipment Facility (GEF-905). The authors would like to thank Mike Craven and two anonymous reviewers for many helpful suggestions to improve the manuscript. We thank Matt King for helpful discussions and Catrin Thomas for assistance during the field campaign.

References

Bombosch, A., and A. Jenkins (1995), Modeling the formation and deposition of frazil ice beneath Filchner-Ronne Ice Shelf, *J. Geophys. Res.*, *100*(C4), 6983–6992.

Chambers, D. (2006), Observing seasonal steric sea level variations with GRACE and satellite altimetry, *J. Geophys. Res.*, *111*, C03010, 10.1029/2005JC002914.

Cook, A. J., and D. G. Vaughan (2010), Overview of areal changes of the ice shelves on the Antarctic Peninsula over the past 50 years, *The Cryosphere*, *4*, 77–98, doi:10.5194/tc-4-77-2010.

Craven, M., F. Carsey, A. Behar, J. Matthews, R. Brand, A. Elcheikh, S. Hall, and A. Treverrow (2005), Borehole imagery of meteoric and marine ice layers in the Amery Ice Shelf East Antarctica, *J. Glaciol.*, *51*(172), 75–84.

Craven, M., I. Allison, H. A. Fricker, and R. Warner (2009), Properties of a marine ice layer under the Amery Ice Shelf, East Antarctica, *J. Glaciol.*, *55*(192), 717–728.

Dierckx, M., and J.-L. Tison (2013), Marine ice deformation experiments: an empirical validation of creep parameters, *Geophys. Res. Lett.*, *40*, 1–5, doi:10.1029/2012GL054197.

Eicken, H., H. Oerter, H. Miller, W. Graf, and J. Kipfstuhl (1994), Textural characteristics and impurity content of meteoric and marine ice in the Ronne Ice Shelf Antarctica, *J. Glaciol.*, *40*(135), 386–398.

Förste, C. (2011), EIGEN-6 - A new combined global gravity field model including GOCE data from the collaboration of GFZ-Potsdam and GRGS-Toulouse; Geophysical Research Abstracts, Vol. 13, EGU2011-3242-2, EGU General Assembly.

Fricker, H. A., S. Popov, I. Allison, and N. Young (2001), Distribution of marine ice beneath the Amery Ice Shelf, *Geophys. Res. Lett.*, *28*(11), 2241–2244, doi:10.1029/2000GL012461.

Glasser, N. F., B. Kulesa, A. Luckman, D. Jansen, E. C. King, P. R. Sammonds, T. A. Scambos, and K. C. Jezek (2009), Surface structure and stability of the Larsen C Ice Shelf, Antarctic Peninsula, *J. Glaciol.*, *55*, 400–410.

Glen, J. W. (1955), The creep of polycrystalline ice, *Proc. R. Soc. London, Ser. A*, *1175*(228), 519–538.

Grosfeld, K., and H. Sandhäger (2004), The evolution of a coupled ice shelf – ocean system under different climate states, *Global Planet. Change*, *42*, 107–132.

Haran, T., J. Bohlander, T. Scambos, T. Painter, and M. Fahnestock, compilers (2005), MODIS Mosaic of Antarctica (MOA) image map. Boulder, Colorado, USA: National Snow and Ice Data Center. Digital Media.

Holland, P. R., and D. L. Feltham (2006), The effects of rotation and ice shelf topography on frazil-laden Ice Shelf Water plumes, *J. Phys. Oceanogr.*, *36*, 2312–2327.

Holland, P. R., H. F. J. Corr, D. G. Vaughan, A. Jenkins, and P. Skvarca (2009), Marine Ice in Larsen Ice Shelf, *Geophys. Res. Lett.*, *36*, L11604, doi:10.1029/2009GL038162.

Holland, P. R., H. F. J. Corr, H. D. Pritchard, D. G. Vaughan, R. J. Arthern, A. Jenkins, and M. Tedesco (2011), The air content of Larsen Ice Shelf, *Geophys. Res. Lett.*, *38*, L10503, doi:10.1029/2011GL047245.

Jansen, D., B. Kulesa, P. R. Sammonds, A. Luckman, E. C. King, and N. F. Glasser (2010), Present stability of the Larsen C Ice Shelf, *J. Glaciol.*, *56*(198), 593–600.

Khazendar, A., and A. Jenkins (2003), A model of marine ice formation within Antarctic ice shelf rifts, *J. Geophys. Res.*, *108*(C7), 3235, doi:10.1029/2002JC001673.

Khazendar, A., J.-L. Tison, B. Stenni, M. Dini, and A. Bondesan (2001), Significant marine-ice accumulation in the ablation zone beneath an Antarctic ice shelf, *J. Glaciol.*, *47*(158), 359–368.

Khazendar, A., E. Rignot, and E. Larour (2009), Roles of marine ice, rheology, and fracture in the flow and stability of the Brunt/Stancomb-Wills Ice Shelf, *J. Geophys. Res.*, *114*, F04007, doi:10.1029/2008JF001124.

Khazendar, A., E. Rignot, and E. Larour (2011), Acceleration and spatial rheology of Larsen C Ice Shelf, Antarctic Peninsula, *Geophys. Res. Lett.*, *38*, L09502, doi:10.1029/2011GL046775.

Kulesa, B., E. C. King, B. E. Barret, D. Jansen, A. J. Luckman, and P. R. Sammonds (2010), Joint inversion of multi-component seismic and ground-penetrating radar (GPR) data for ice-physical properties, and application to the Larsen C Ice Shelf. EOS, Transactions of the American Geophysical Union, Fall Meeting Supplement (December 2010).

Larour, E., E. Rignot, I. Joughin, and D. Aubry (2005), Rheology of the Ronne Ice Shelf, Antarctica, inferred from satellite radar interferometry data using an inverse control method, *Geophys. Res. Lett.*, *32*, L05503, doi:10.1029/2004GL021693.

Lenaerts, J. T. M., M. R. van den Broeke, W. J. van den Berg, E. van Meijgaard, and P. Kuipers-Munneke (2012), A new, high-resolution surface mass balance map of Antarctica (1979–2010) based on regional atmospheric climate modeling, *Geophys. Res. Lett.*, *39*, L04501, doi:10.1029/2011GL050713.

Lewis, E. L., and R. G. Perkin (1986), Ice pumps and their rates, *J. Geophys. Res.*, *91*(C10), 11,756–11,762.

Luckman, A., D. Jansen, B. Kulesa, E. C. King, P. Sammonds, and D. I. Benn (2012), Basal crevasses in Larsen C Ice Shelf and implications for their global abundance, *Cryosphere*, *6*, 113–123, doi:10.5194/tc-6-113-2012.

Lythe, M. B., D. G. Vaughan, and the BEDMAP Consortium (2001), BEDMAP: A new ice thickness and subglacial topographic model of Antarctica, *J. Geophys. Res.*, *106*(B6), 11,335–11,351.

MacAyeal, D. R., S. Shabtaie, C. R. Bentley, and S. D. King (1986), Formulation of ice shelf dynamic boundary conditions in terms of Coulomb rheology, *J. Geophys. Res.*, *91*(B8), 8177–8191.

MacAyeal, D. R., E. Rignot, and C. L. Hulbe (1998), Ice-shelf dynamics near the front of the Filchner-Ronne Ice Shelf, Antarctica, revealed by SAR interferometry: model/interferogram comparison, *J. Glaciol.*, *44*(147), 419–428.

Massom, R. A., et al. (2001), Snow on Antarctic sea ice, *Rev. Geophys.*, *39*(3), 413–445.

McGrath, D., K. Steffen, T. Scambos, H. Rajaram, G. Casassa, and J. L. Rodriguez Lagos (2012), Basal crevasses and associated surface

- crevassing on the Larsen C Ice Shelf, Antarctica and their role in ice-shelf instability, *Ann. Glaciol.*, 53(60), 10–18, doi:10.3189/2012AoG60A005.
- Morgan, V. I. (1972), Oxygen Isotope Evidence for Bottom Freezing on the Amery Ice Shelf, *Nature*, 238, 393–394, doi:10.1038/238393a0.
- Neal, C. S. (1979), The dynamics of the Ross Ice Shelf, revealed by radio echo-sounding, *J. Glaciol.*, 24(90), 295–307.
- Nicholls, K. W., H. F. J. Corr, K. Makinson, and C. J. Pudsey (2012), Rock debris in an Antarctic ice shelf, *Ann. Glaciol.*, 53(60), doi:10.3189/2012AoG60A014.
- Oerter, H., J. Kipfstuhl, J. Determann, H. Miller, D. Wagenbach, A. Minikin, and W. Graf (1992), Evidence for basal marine ice in the Filchner-Ronne ice shelf, *Nature*, 358, 399–401.
- Paterson, W. S. B. (1994), *The physics of glaciers*, 3rd ed., 235–236, Elsevier, Oxford.
- Pattyn, F., K. Matsuoka, D. Callens, H. Conway, M. Depoorter, D. Docquier, B. Hubbard, D. Samyn, and J. L. Tison (2012), Melting and refreezing beneath Roi Baudouin Ice Shelf (East Antarctica) inferred from radar, GPS, and ice core data, *J. Geophys. Res.*, 117, F04008, doi:10.1029/2011JF002154.
- Rignot, E., J. Mouginot, and B. Scheuchl (2011), MEaSURES InSAR-Based Antarctica Ice Velocity Map. Version 1. Boulder, Colorado USA: National Snow and Ice Data Center.
- Sandhäger, H. (2000), Quantifizierung eisdynamischer und massenhaushaltsrelevanter Basisgrößen eines Antarktischen Inlandeis-Schelfeis-Systems unter Einsatz eines numerischen Fließmodells, PhD-thesis, Universität Münster, Germany.
- Sandhäger, H., W. Rack, and D. Jansen (2005), Model investigations of Larsen B Ice Shelf dynamics prior to the breakup, Forum for Research into Ice Shelf Processes (FRISP), Report, 16, 5–12, Bjerknes Cent. ForClim. Res., Bergen, Norway.
- Scambos, T. A., C. Hulbe, M. Fahnestock, and J. Bohlander (2000), The missing link between climate warming and break-up of ice shelves in the Antarctic Peninsula, *J. Glaciol.*, 46(154), 516–530.
- Thyssen, F. (1988), Special aspects of the central part of Filchner-Ronne Ice Shelf, Antarctica, *Ann. Glaciol.*, 11, 173–179.
- Tison, J., R. Souchez, E. W. Wolff, J. C. Moore, M. R. Legrand, and M. de Angelis (1998), Is a periglacial biota responsible for enhanced dielectric response in basal ice from the Greenland Ice Core Project ice core?, *J. Geophys. Res.*, 103(D15), 18,885–18,894, doi:10.1029/98JD01107.
- Tison, J.-L., A. Khazendar, and E. Roulin (2001), A two-phase approach to the simulation of the combined isotope/salinity signal of marine ice, *J. Geophys. Res.*, 106(C12), 31,387–31,401, doi:10.1029/2000JC000207.
- Treverrow, A., R. C. Warner, W. F. Budd, and M. Craven (2010), Meteoric and marine ice crystal orientation fabrics from the Amery Ice Shelf, East Antarctica, *J. Glaciol.*, 56(199), 877–890.
- Vaughan, D. G., D. R. Mantripp, J. Sievers, and C. S. M. Doake (1993), A synthesis of remote sensing data on Wilkins Ice Shelf Antarctica, *Ann. Glaciol.*, 17, 211–218.
- Warren, G. S., C. S. Roesler, V. I. Morgan, R. E. Brandt, I. D. Goodwin, and I. Allison (1993), Green icebergs formed by freezing of organic-rich seawater to the base of Antarctic ice shelves, *J. Geophys. Res.*, 98(C4), 6921–6928.